Tunable photonic devices by 3D laser printing of liquid crystal elastomers

SIMON WOSKA,[1,*] ALEXANDER MÜNCHINGER,[1] DOMINIK BEUTEL,[2] EVA BLASCO,[3,4] JANNIS HESSENAUER,[1] OSMAN KARAYEL,[1] PASCAL RIETZ,[1] STEFAN PFLEGING,[1] ROMAN OBERLE,[1] CARSTEN ROCKSTUHL,[2,3] MARTIN WEGENER,[1,3] AND HEINZ KALT[1]

[1]*Institute of Applied Physics, Karlsruhe Institute of Technology (KIT), 76131 Karlsruhe, Germany*
[2]*Institute of Theoretical Solid State Physics, Karlsruhe Institute of Technology (KIT), 76131 Karlsruhe, Germany*
[3]*Institute of Nanotechnology, Karlsruhe Institute of Technology (KIT), 76344 Eggenstein-Leopoldshafen, Germany*
[4]*Institute for Chemical Technology and Polymer Chemistry (KIT), 76131 Karlsruhe, Germany*
*simon.woska@kit.edu

Abstract: Liquid crystal elastomers (LCEs) are highly suitable materials for the fabrication of flexible photonic elements due to their ability for directional actuation induced by external stimuli. 3D laser printing (3DLP) is a well-established method to realize complex photonic architectures. In this paper, we present the technological adaptations necessary to combine the actuation-controlled flexibility of LCE with the design options inherent to 3DLP to realize a platform for tunable photonics. The role of birefringence of the LCE in the 3DLP fabrication is addressed and theoretically modelled. We demonstrate how LCEs can be used both as a flexible substrate for arrays of rigid photonic elements and as a material for tunable photonic structures itself. Flexible coupling of two optical whispering gallery mode cavities and full spectral tunability of a single cavity are presented as exemplary applications.

1. Introduction

Photonic building blocks on the micro and nano scale, such as optical filters or sensors, are central elements of modern optoelectronics [1,2]. Such systems are also highly suitable for fundamental investigations, e.g., of cavity quantum dynamics or topological effects [3,4]. Most of these structures are based on semiconductor materials [5–7], but photonic elements made from polymers have recently been established as interesting alternatives [8–10].

The reasons for this development are obvious. Polymers are compatible with state-of-the-art lithography technologies [9–12] and have the potential for low-cost up-scaling to large production numbers using nanoimprint lithography [13,14]. Optical parameters like refractive indices or thermo-optical coefficients can be adjusted to specific requirements thanks to the abundance of available polymers and polymer blends [15–18]. Quantum emitters, such as quantum dots or organic laser dyes, can be integrated to realize active optical elements [19,20]. Also surface functionalization is feasible for applications in bio-medical sensing [21].

A major advantage with respect to semiconductors or glasses is the mechanical flexibility of a specific polymer class called elastomers. On the macro scale, they are used as substrate or host material for photonic structures made from rigid polymers. Application of mechanical stress induces changes of the elastomers' shape, which has been employed to achieve tunability of distributed feedback (DFB) devices [22–26] or whispering gallery mode (WGM) micro droplet lasers [27]. Our group has established some key elements of photonic cavity arrays namely fully tunable disk-shaped WGM cavities as well as photonic molecules with flexible coupling [28,29].

It would be of great advantage to transfer the addressed merits of flexibility to the micro scale. However, this step requires elastomer structures that can be triggered by stimuli other than by direct mechanical stress. Promising candidates to achieve this goal are liquid crystal elastomers (LCEs). These polymers reversibly respond to various external stimuli, e.g., temperature, optical excitation, or electric/magnetic fields by means of a pre-defined mechanical actuation within a few ms [30]. Changes of the LCEs' shape can be triggered in a controlled way by perturbing the directional order of the rod-shaped mesogens of the polymeric network [31]. LCEs are widely used as actuators on the macro scale [32,33] as well as in micro robotics [30,34,35]. First experiments on the micro scale demonstrated the tunability of hybrid goblet-shaped WGM cavities [36] or LCE ring resonators [37].

Fabrication of micron-size LCE photonic elements is challenging using standard methods of lithography. On the other hand, 3D laser printing (3DLP), i.e., using multi-photon polymerization induced by tightly focused fs-laser pulses, allows for the manufacturing of nearly arbitrary structures from various polymers with sub-micron resolution [38]. What remains as a challenge is to realize high-resolution photonic structures with sufficient mesogen alignment within the LCE.

In this paper, we report on the adaptions of the state-of-the-art 3DLP process necessary when using liquid crystal elastomers. At first, we focus on the realization of rigid photonic elements fabricated on micro scale LCE substrates. Here, the stimulation of the LCE enables to modulate the distance and thus the coupling between the photonic elements. We address the substrates' fabrication process and the adapted 3DLP configuration for the subsequent production of rigid structures on these substrates. We also introduce a 3DLP-based investigation scheme for testing the LCE substrates' actuation strength. At second, we cover the fabrication of photonic structures entirely made from LCE. We theoretically describe the implications of the LCEs' birefringence and how to tackle this problem by modification of the 3DLP fabrication process. The successful application of our newly developed approaches towards tunable photonics is demonstrated by fiber-based transmission spectroscopy of polymeric whispering gallery mode cavities near the infrared (IR) c-band.

2.   3D laser printing of rigid building blocks on flexible LCE substrates

2.1.   Fabrication of substrates made from LCE

Following the approach presented here, cylindrical liquid crystal elastomer substrates with a thickness of a few tens of μm and diameters of a few hundred μm were produced via one-photon polymerization. These substrates can be used to reversibly control the distance between rigid elements fabricated onto them by 3DLP, as schematically depicted in Fig. 1. A sufficient in-plane mesogen alignment of the substrates allows for a simultaneous contraction (parallel to alignment) and expansion (perpendicular to alignment) behavior and was achieved by sandwiching the LCE resist between polymeric sacrificial layers covered with parallel micro scratches.

The LCE substrates were fabricated from a resist consisting of 79 mol% of the mesogen 4-methoxybenzoic acid 4-(6-acryloyloxy-hexyloxy)phenyl ester, 20 mol% of the crosslinker molecule 1,4-bis[4-(3-acryloyloxypropoxy)benzoyloxy]-2-methylbenzene (both SYNTHON Chemicals GmbH & Co. KG, Bitterfeld-Wolfen, Germany), and 1 mol% of the photoinitiator 2-benzyl-2-(dimethylamino)-4'-morpholinobutyrophenone (Irgacure 369, Sigma-Aldrich Chemie GmbH, Munich, Germany), based on [34]. The components were magnetically stirred at 80 °C for at least 24 h. Afterwards, the resist was filled into a cell by capillary forces on a heat plate at 80 °C.

The cell was formed by two 22×22 mm^2 cover glasses (Carl Roth GmbH + Co. KG, Karlsruhe, Germany) coated with different polymeric sacrificial layers. The cell's thickness was defined to be approximately 30 μm using adhesive spacer foil CMC 10764 (CMC Klebetechnik GmbH, Frankenthal, Germany). The upper sacrificial layer was made from polyvinyl alcohol (Mowiol
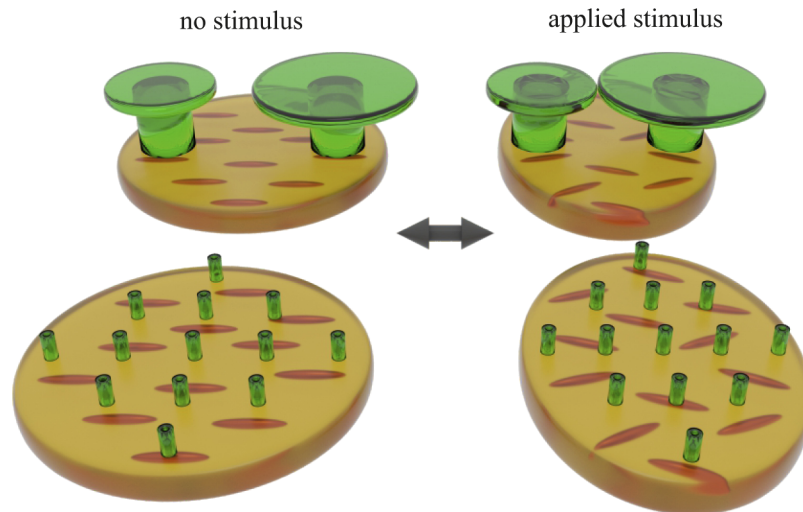
Fig. 1. Schematic illustration of rigid 3DLP structures on actuating LCE substrates without (left) and with (right) applied external stimulus. 2D arrays of rigid markers are used to evaluate the contraction/expansion mechanism of LCE substrates parallel/perpendicular to the mesogen alignment direction (front). As an exemplary application, the substrate's contraction can be used to flexibly and reversibly couple pairs of disk-shaped WGM resonators, if the axis of the resonator pair is oriented parallel to the alignment direction (back).

4-88, Sigma-Aldrich Chemie GmbH, Munich, Germany) dissolved to saturation in deionized water. The solution was spin-coated onto the previously aceton- and isopropanol-cleaned and N_2-dried cover glass at 1200 rpm for 60 s and baked on a heat plate at 80 °C for 120 s. As sacrificial layer on the lower cover glass, a polyimide based on 3,3',4,4'-benzophenonetetracarboxylic dianhydride and 3,3'-dimethyl-4,4'-diaminodiphenyl methane was used [39]. To this end, the cover glass was cleaned using aceton, isopropanol and N_2, dried on a heat plate at 180 °C for 10 min and afterwards activated using an oxygen plasma treatment (NanoB, Diener electronic GmbH Co. KG, Ebhausen, Germany) for 2 min at 30 W with a pressure of 0.3 mbar and an oxygen flow of 10 sccm. After a second drying step at 180 °C for 10 min, a poly(amic acid) was spincoated onto the cover glass. Afterwards the polyimide was thermally imidized via a 6-step baking procedure. The process of the synthesis, spincoating and baking was adapted from [39]. Both sacrificial layers were then rubbed with a velvet cloth using a custom built tool (adapted from [40]) to trigger an in-plane mesogen alignment of the LCE via parallel micro scratches.

The cell with infiltrated LCE resist was then cooled to room temperature over several hours and illuminated with a custom built UV lamp ($\approx 3\,\text{mW cm}^{-2}$ at 375 nm) for 20 s through a mask to polymerize small substrates. Afterwards, the cell was opened by dissolving the polyvinyl alcohol layer in deionized water and the substrates were developed in 1-methoxy-2-propanol acetate (PGMEA) for at least 15 min, isopropanol-rinsed and N_2-dried.

Following this recipe, we were able to fabricate LCE substrates with a thickness of $\approx 30\,\mu\text{m}$ and a diameter of $\approx 300\,\mu\text{m}$ as exemplary depicted in the scanning electron microscopy (SEM) micrograph in Fig. 2(a). Although the substrate does show the expected dimensions and cylindrical shape, small imperfections on its surface are apparent, which are one of the major challenges when printing 3DLP structures on these substrates.

2.2. Verification of the directional actuation of LCE substrates

Freestanding LCE micro structures have been shown to undergo a relative contraction of up to 20 % under optical pumping [30]. For micro scale applications, it is essential that similar contraction behavior also occurs for surface-bound substrates. In the following, we introduce a method to evaluate the contraction strength of LCE substrates based on 3DLP. Using this evaluation, the substrates' fabrication parameters can be engineered and the feasibility of LCE-based photonic building blocks is estimated.

The adhesion of an LCE substrate to a planar surface partly prevents its actuation mechanism. This effect could be counteracted by using thicker substrates, but only at the expense of decreasing alignment and therefore reducing the overall actuation strength, since the alignment forces induced by the rubbed sacrificial layers decrease with increasing distance from these layers [41]. Consequently, the feasibility of applications based on LCE substrates on the micro scale needs to be evaluated regarding the substrates' actuation strength. To characterize the locally different actuation behavior, a two-dimensional grid of markers with lattice vectors parallel/perpendicular to the mesogen alignment direction was structured onto the LCE substrates using 3D laser printing. Hence, the contraction/expansion of the substrates can be evaluated via the change of the distance between the markers parallel/perpendicular to the alignment direction under an external stimulus like a thermal treatment. A scheme of this approach is depicted in the foreground of Fig. 1.

The markers were structured as a square array with a period of 40 μm of hollow cylinders with an outer radius of 3 μm and an inner radius of 1 μm, since this shape is well suited for the follow-up processing of microscopic images. As all rigid structures on LCE substrates within this work, the grids were printed from the commercial negative-tone resist IP-S using the 3DLP system Photonic Professional GT (both Nanoscribe GmbH, Eggenstein-Leopoldshafen, Germany). The 3DLP system focuses an fs-pulsed excitation laser beam with pre-defined polarization into the photoresist using a 63× microscope objective with a numerical aperture of 1.4. As light source, a frequency doubled erbium fiber laser with a center wavelength of 780 nm, a repetition rate of 80 MHz and a pulse width < 100 fs is used. The structures were printed in the so-called sandwich configuration. Herein, they are produced upside down to prevent the excitation laser's beam from passing the substrate before polymerizing the resist. One important challenge within this process is the reliable adhesion of the markers with footprints of only around 25 μm^2 on the imperfect surface of the LCE substrate. Additionally, all upper ends of the markers need to be on the same height, to enable a simultaneous high-resolution imaging of all markers within one focal plane. To this end, for each marker the path of the excitation laser's focus is chosen to begin 5 μm below the substrate/resist interface detected at the beginning of the 3DLP process. Consequently, all markers are attached to the substrate's surface, despite eventual variations of the substrate height or overall sample tilts. To guarantee a high degree of crosslinking of the markers at the LCE surface while preventing the formation of micro bubbles due to explosions, 3DLP fabrication parameters have to be carefully engineered. The markers in this paper (as exemplarily depicted in Fig. 2(a)) were structured with a scan speed of 1 cm s^{-1} and a relative laser power of 75 %. Within this work, relative laser powers refer to a power of around 50 mW measured at the back focal plane of the 3DLP system.

To evaluate the actuation of a substrate, microscopic images are taken at different temperatures, controlled by means of a Peltier element (European Thermodynamics Ltd., Leicestershire, UK), a Pt100 temperature sensor (Heraeus Holding GmbH, Hanau, Germany) and a proportional–integral–derivative controller (Red Lion, York PA, USA). A routine based on MATLAB is then used to detect the markers on the microscopic images and calculate the relative change of the distances between their centers. The precision of the algorithm used to determine the distances between two markers is expected to be in the order of the pixel size of the microscopic images. This leads to a precision of the determined relative distance changes of around 0.5 %, although the precision of the material deformation itself is expected to be significantly higher.
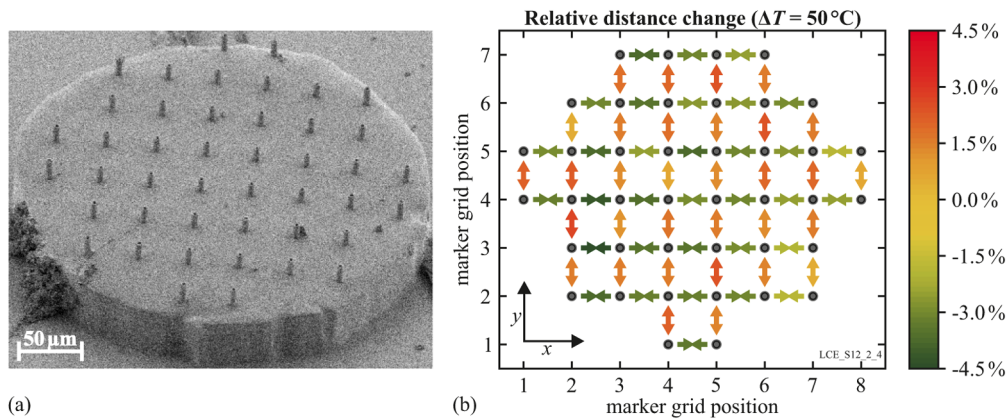
Fig. 2. (a) SEM micrograph of markers structured on an LCE substrate with a next-neighbor distance of 40 μm. (b) Investigation of the directional actuation of a substrate with mesogen alignment along the *x*-axis: The arrows between two markers (dark circles) show the relative change of the distance between the markers under a temperature change from $T = 22\,°C$ to $T = 72\,°C$ via their color code. Despite the varying actuation strength between the different areas of the substrate, a clear directional actuation with local contractions of over 4 % and expansions of around 3 % is visible.

An exemplary result of such an evaluation is depicted in Fig. 2(b). A clear directionality with contraction/expansion of several percent parallel/perpendicular to the mesogen alignment direction is found. Furthermore, a varying actuation strength at different areas of the substrate can be detected following this investigation scheme. The absolute contraction/expansion values could be further increased by heating the substrate to higher temperatures. Eventually, they are limited by the substrate's adhesion to the glass surface.

Following the presented approach, the actuation strength of micro scale LCE substrates was successfully evaluated and the feasibility of building blocks based on the required actuation strength and the intended stimulus can be estimated. Since the absolute values of the distance changes also strongly depend on material and production parameters of the LCE substrate, the evaluation can also be used for engineering the substrate's fabrication process to further increase the actuation strength.

2.3. Tunable evanescent coupling of whispering gallery mode resonators

Next, as an exemplary application of tunable photonic building blocks on micro scale LCE substrates, we demonstrate the flexible evanescent coupling of two disk-shaped WGM cavities. We first give insight into the cavities' fabrication process and then prove the flexible evanescent coupling of two cavities by means of fiber-based transmission spectroscopy under a thermal treatment.

Tunable coupling of WGM resonators has previously been realized using independent substrates on micro-manipulators [42,43] or macro scale PDMS substrates [29] and can be used to create tunable coupled-resonator optical waveguides [44,45] as well as to investigate fundamental concepts like exceptional points in hybrid coupled systems [43,46,47]. To realize such tunable coupling, disk-shaped, size-mismatched WGM resonators (with radii $R_1 \approx 20\,μm$, $R_2 \approx 30\,μm$) were printed in close proximity onto an LCE substrate using 3DLP in sandwich configuration. Hereby, both disks and pedestals are fabricated from IP-S and therefore could be produced in a one-step process. Precisely and reversibly tunable coupling can then be initiated using various external stimuli such as, e.g., a thermal treatment.

The minimal initially achievable gap between two resonator disks is not only limited by the 3DLP's resolution [48], but also by the photoresist's shrinkage and swelling behavior during the development process. While shrinkage generally decreases the size of the polymeric structures and therefore increases the inter-cavity gap, swelling of the material by absorption of the organic developer can lead to contact of the disks while developing. This aspect is critical for structures on LCE substrates, since although the swelling recedes while sample drying, a tilt of the resonator pedestals due to the substrates flexibility and adhesive forces between the disks can occur. These forces can result in the dried structures still being in contact. The disk's in-plane shrinkage can be minimized by engineering the fabrication parameters to ensure a maximum degree of crosslinking while preventing micro explosions. The WGM resonators presented here were structured using a laser power of 54 % and a scan speed of $1 \, \mathrm{cm \, s^{-1}}$ and were developed in PGMEA for at least 45 min. Combining these parameters with an nominal gap size of $1.3 \, \mu\mathrm{m}$, room temperature inter-cavity gaps smaller than $2 \, \mu\mathrm{m}$ have been achieved (see microscopic images in Fig. 3(a)).
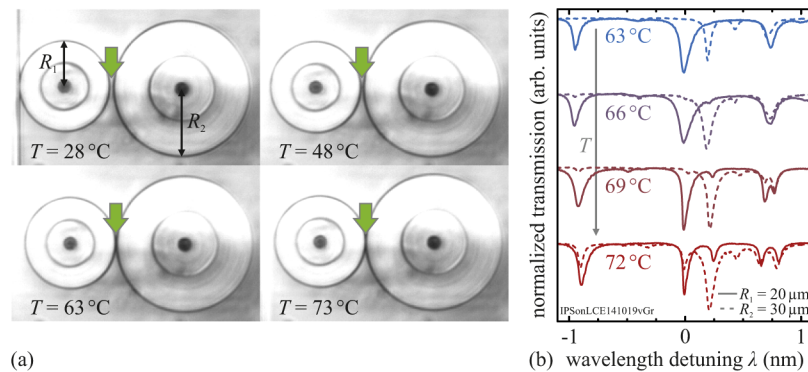

Fig. 3. (a) Microscopic images of two rigid size-mismatched WGM resonators (with radii $R_1 \approx 20 \, \mu\mathrm{m}$, $R_2 \approx 30 \, \mu\mathrm{m}$) on an LCE substrate at different temperatures. While at low temperatures an inter-cavity gap (green arrow) of around $2 \, \mu\mathrm{m}$ is visible, the gap size is below the resolution limit at high temperatures. (b) Fiber-based transmission spectra of both resonators at different temperatures, corrected for thermo-optic mode shifts by aligning a clearly identifiable resonance (at 1516.58 nm for $T = 63 \, ^\circ\mathrm{C}$) at zero detuning for all temperature steps. While the spectra of both cavities seem to be uncorrelated at low temperatures, resonant modes of one resonator appear in the other resonator's spectrum with increasing temperature, and vice versa. The mode resonant in both cavities at around 0.8 nm wavelength detuning shows a clear splitting behavior at elevated temperatures.

Since efficient evanescent coupling of optical WGMs requires inter-cavity gaps smaller than around half the wavelength of the light [49,50], the resonators are uncoupled after the manufacturing process. Hence, the contracting mechanism of LCE substrates has to be utilized to realize a flexible coupling of the cavities, as depicted in the background of Fig. 1. Comparing the realized gap sizes with the disks' center distance of around $50 \, \mu\mathrm{m}$, the contraction strength of the LCE substrates investigated in Fig. 2(b) is sufficient to couple the resonators by heating to moderate temperatures.

To verify tunable coupling of the cavity modes, temperature-dependent fiber-based transmission spectroscopy measurements were conducted. The temperature was controlled as described above. At each temperature step, a tapered optical fiber (Corning SMF-28, tapered to a minimum diameter of around $1 \, \mu\mathrm{m}$ based on [51]) is brought in close proximity with each of the cavities consecutively to enable evanescent coupling between resonator and fiber. Light from an external cavity diode laser near the IR c-band (CTL, TOPTICA Photonics, Gräfelfing, Germany) is transmitted through the fiber and detected via a photo diode after passing the resonator. Resonant

WGMs appear as Lorentz-shaped dips in the fiber's transmission spectrum when scanning the wavelength of the incoupled IR light.

An exemplary measurement of tunably coupled WGMs is presented in Fig. 3. Figure 3(a) depicts the visible change of the size of the inter-cavity gap between two resonators with varying temperature, while Fig. 3(b) shows temperature-dependent fiber-based transmission spectra of both resonators. At low temperatures, the spectra of both resonators seem to be uncorrelated, while at elevated temperatures a clear correlation between the spectra arises. Modes which were initially only resonant in one of the cavities now appear in both spectra since the two resonators form a coupled system at high temperatures. Some modes also show a clear splitting behavior, as exemplarily shown at a wavelength detuning of around 0.8 nm. Such mode splitting can be explained by non-degenerate binding and anti-binding supermodes localized over the whole system, which are well-known in coupled resonator pairs [42].

Based on these findings, we have successfully demonstrated a tunable evanescent coupling of two WGM cavities on an LCE substrate using a thermal treatment as an external stimulus. Hereby, the cavity modes were reversibly coupled by heating the system up to around 70 °C. This application demonstrates the suitability of the 3D laser printing process for fabricating rigid photonic elements onto flexible LCE substrates on the micro scale. In addition, we have shown the strong potential of flexible photonic building blocks based on LCE substrates.

3. 3D laser printing of photonic building blocks made from LCE

In the following, we address the 3D laser printing of high-resolution photonic elements entirely made from LCE, since such structures promise a large tuning range of their geometrical and optical properties. At first, we investigate the influence of the birefringence of photoresists within the context of 3DLP by simulations of the light path of the fs-pulsed excitation laser. Based on these findings, an adaption of the conventional 3DLP configuration is presented. As an exemplary application of this new fabrication approach, a fully tunable whispering gallery mode resonator entirely made from LCE is produced.

3.1. Simulation of the 3DLP focal shape in birefringent resists

In contrast to photoresists typically used for 3DLP, LCEs can be strongly birefringent. Birefringence is expected to cause two spatially separated foci and consequently a simultaneous polymerization of two voxels. Clearly, two separate foci are unwanted in the context of 3D laser printing high-resolution photonic structures. To get further understanding of this issue, we here present corresponding numerical calculations.

The considered system consists of the objective lens that focuses a circularly polarized beam with Gaussian shape at a center wavelength of 780 nm into the photoresist. We consider, according to the experimental situation, immersion oil behind the lens. A 170 μm thick cover glass separates the immersion oil from the resist, which is considered as an infinite half space. The resist is birefringent and the extraordinary axis is aligned with the optical axis of the whole system, which is taken as the *z*-axis. The simulation uses a two-step process [52,53]. First, the field distribution behind the objective lens is computed using the Richards-Wolf method [54]. Second, the propagation of the field through the layered, birefringent medium is calculated with the 4-by-4 matrix method [55,56].

We use the Richards-Wolf method as follows: The field of the excitation beam is refracted at a reference sphere, which is defined by the lens parameters, onto the focal spot of the lens. This field is then decomposed into its angular spectrum. The numerical aperture of $NA = 1.4$ defines a maximum angle for this decomposition. Each plane wave component of the angular spectrum propagates through the materials along the optical path of the 3DLP system, consisting of the immersion oil, the cover glass, and the birefringent resist. This problem is solved with the 4-by-4

matrix method. Here, the wave equation

$$\left(\mathbf{k} \times \mathbf{k} \times + \frac{\omega^2}{c_0^2} \epsilon_i\right) \mathbf{E} = 0 \tag{1}$$

for the electric field $\mathbf{E}$ at angular frequency ω is solved for each material layer in the stack. The material properties are defined by their respective relative permittivity ϵ_i. In the case of a birefringent medium, the permittivity is a tensor. The speed of light in vacuum is c_0 and we assume unity for the permeabilities of the material. Additionally, the x- and y-components of the wave vector $\mathbf{k} = (k_x, k_y, k_z)^\mathrm{T}$ are fixed. We assume that the media are infinitely extended in the x-y-plane, such that these tangential components are conserved throughout the system due to translational invariance. The eigenmodes are found by searching for values k_z for which the term in brackets in (1) has a non-trivial kernel, i.e., a vanishing determinant. The determinant of the term in brackets leads to a fourth-order polynomial in k_z and thus to four solutions: two polarizations each for the forward and the backward propagating light.

Having found the four modes in each material, the interface conditions at the transition between the different media can be enforced to propagate the field from one layer to the next one. The solution is encoded in the multiplication by a 4-by-4 transfer matrix, relating the modes in the medium of the incident wave with those in the medium of the transmitted wave. Now, each mode of the angular spectrum propagates through the stack by subsequent matrix multiplications. Having the expansion of the electric field in the eigenmodes of each medium, the angular spectrum is available throughout the stack. To compute the electric field at a specified point, the integral over the angular spectrum is calculated by numerical quadrature.

For the simulation of the 3D laser printing system, the lens is described by its numerical aperture of 1.4 and a magnification of 63. The illuminating beam has a Gaussian cross section with a width of 5 mm and a circular polarization. The stack through which the light is focused consists of the immersion oil with $\epsilon = 1.518^2$ and a cover glass with $\epsilon = 1.523^2$. The glass has a thickness of 170 μm. Finally, the light is focused into the birefringent resist. Hereby, permittivities of $\epsilon_\mathrm{o} = 1.497^2$ and $\epsilon_\mathrm{e} = 1.675^2$ [57–60] along the ordinary and extraordinary axis, respectively, are assumed. This configuration corresponds to the experimental situation presented in sec. 3.2. We probe 50 different depths of the ordinary focus in the birefringent material. For each simulation, we calculate the intensity in the x-z-plane within the photoresist, using an angular spectrum that is resolved with 120 azimuthal and 120 polar angles for the integration. The intensity has rotational symmetry around the z-axis due to the rotational symmetry of the system and the circularly polarized incoming beam. Thus, the x-z-plane contains the full information of the focal spot position. The position of these spots is calculated by fitting simultaneously two 2D-Gaussian functions to the intensity using least squares. The maxima of these Gaussians are taken as the position of the ordinary and extraordinary focal spot. Figure 4 shows the separation s of the extraordinary and the ordinary focus, taking the depth d of the ordinary focus in the resist as reference. Depth and separation show an approximately linear dependence. For short distances, the overlap of the foci and distortions due to interference effects renders the determination of the focus positions less robust. Thus, we excluded data points with a focus separation below 2.5 μm from the linear regression. The simulation results in a separation of the foci of 0.30 times the depth of the ordinary focus.

To test the robustness of this result with respect to uncertainties in the parameters, we performed several runs with varied parameters. The width of the Gaussian beam was increased and decreased by 20 %. This results in linear fits of $s(d) = 0.30 \times d + 0.17$ μm and $s(d) = 0.30 \times d + 0.24$ μm for the wider and narrower beams, respectively. Furthermore, the refractive indices of the photoresist were varied by 5 %. This results in four different configurations: both indices being smaller, both indices being larger, and the indices being farther away from each other. In these cases, the calculated slopes are 0.30, 0.27, and 0.61, respectively. For the case of closer values, the
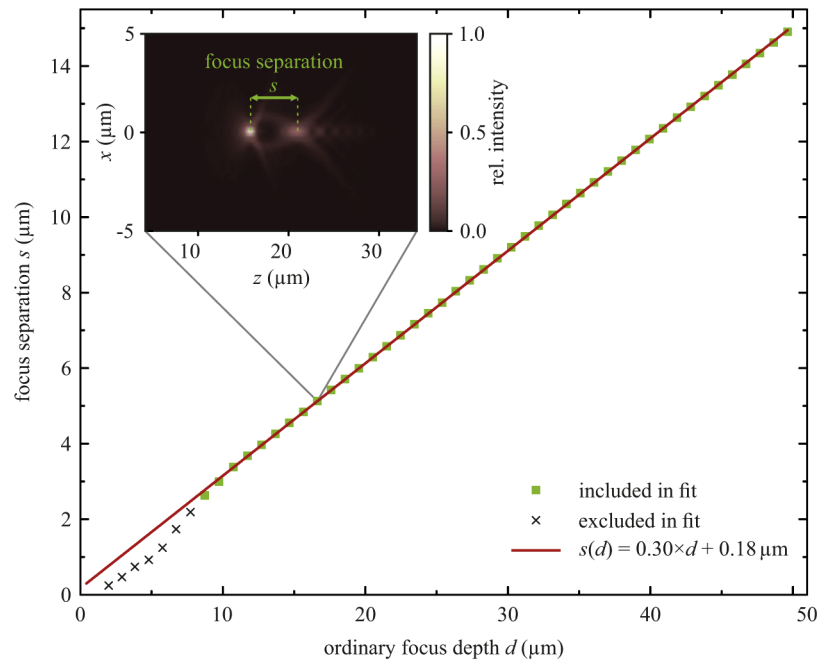
Fig. 4. Simulated focus separation *s* between the ordinary and extraordinary focus of the 3D laser printing system in the birefringent LCE photoresist. For ordinary focus depths *d* up to approximately 50 μm, we observe a linear dependency with a slope of 0.30. The positions of the foci are determined by simultaneously fitting two Gaussian functions to the two-dimensional intensity distribution. Such a distribution is exemplarily shown in the inset. For separations below 2.5 μm, the determination of the focus positions is not precisely possible due to strong interference. Therefore, we excluded those data points from the linear fit.

birefringent properties are not very pronounced and the foci always overlap in the probed depth range. These result shows that, although they are slightly varying under different parameter settings, both the linear dependency as well as the order of magnitude of the calculated slope are robust under the investigated parameter uncertainties.

Based on the findings from the conducted simulations, we conclude that depending on the feature size and the resolution of the printing system, the focus depth must not be increased beyond a certain point to avoid a distorted focus or multiple foci. To achieve this goal, the conventional 3DLP configuration has to be adapted to enable the fabrication of high-resolution elements made from LCE. One possible approach within this context in presented in the following.

3.2. Fabrication of photonic structures made from LCE

The fabrication approach presented here enables the printing of high-resolution photonic elements entirely made from LCE. Based on the findings in sec. 3.1, the conventional 3DLP configuration is adapted for that purpose. Similar to the fabrication of LCE substrates in sec. 2.1, a sufficient mesogen alignment of photonic structures made from LCE is created by sandwiching the resist between two cover glasses. This time, an alignment direction vertical to the glass surfaces is generated by alignment forces due to mono-layers of silane on both cover glasses.

To guarantee the generation of a sufficient mono-layer of silane on their surfaces, the cover glasses were thoroughly cleaned using the alkaline and acidic glass cleaners deconex OP 146, OP 121 and OP 171 (all Borer Chemie AG, Zuchwil, Switzerland) in an ultrasonic cleaner at 70 °C.

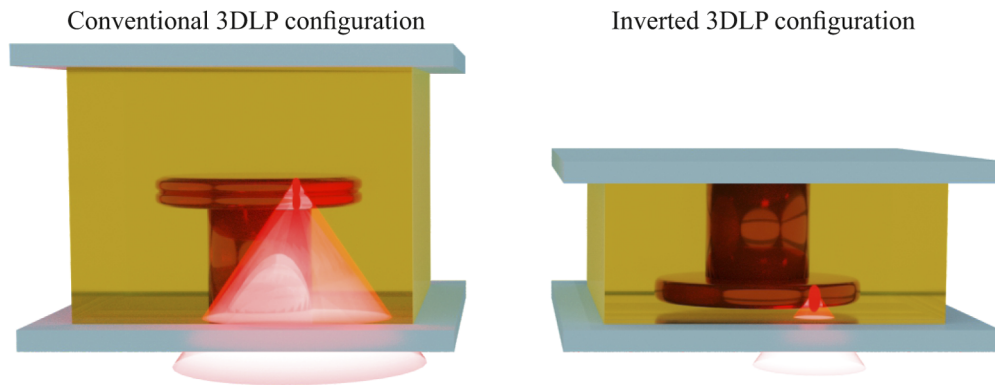Conventional 3DLP configuration   Inverted 3DLP configuration

Fig. 5. Schematic illustration of the adapted 3DLP process. Following the conventional fabrication approach on the left-hand side, the resonators show a strong double-disk character due to the resist's birefringence and the large focus depth of the excitation laser beam. This issue can be overcome following our inverted fabrication approach on the right-hand side, where the focus depth is minimized by inverting the *z*-axis and adapting the cell's thickness to match the height of the LCE structure. See Fig. 6 for SEM micrographs of cavities fabricated following the two approaches.

(Cleaning process adapted from Schott AG, Mainz, Germany.) After drying in a convection oven at 150 °C for 1 h, the glasses were activated in an oxygen plasma (see sec. 2.1 for details) and silanized in a solution of 0.025 vol% dimethyloctadecyl[3-(trimethoxysilyl)propyl]ammonium chloride (DMOAP) and 0.157 vol% 3-(trimethoxysilyl)propyl methacrylate (both Sigma-Aldrich Chemie GmbH, Munich, Germany) in toluene for 20 min. The two different silanes are used to generate alignment and adhesion of the LCE structures, respectively. After cleaning for 5 min in pure toluene, the glasses were dried at 90 °C for 1 h. Similar to sec. 2.1, the LCE resist was then infiltrated into a cell made from two cover glasses and adhesive spacer foils on a heat plate at 80 °C. After cooling to room temperature over several hours, polymerization via multi-photon absorption was initiated using the same 3DLP system as described above [61]. The subsequent development was done in a 50:50 mixture of aceton and isopropanol for 15 min.

The LCE resist is made of 40 wt% of the mixture described in sec. 2.1 (but using the photoinitiator bis(2,4,6-trimethylbenzoyl)-phenylphosphineoxide, Irgacure 819, Sigma-Aldrich Chemie GmbH, Munich, Germany) and 60 wt% of the liquid crystal (LC) host E7 (SYNTHON Chemicals GmbH & Co. KG, Bitterfeld-Wolfen, Germany), adapted from [62]. The eutectic nematic LC host material promotes the alignment of the LCE mesogens and lowers the melting point of the resist below room temperature, leading to a strong enhancement of both the mesogen alignment as well as the shape quality of the LCE structures polymerized by 3DLP. Since the LC mesogens are not part of the LCE network after polymerization, they are washed out during the development process. This leads to a strong shrinkage behavior, which has to be taken into account.

As simulated in sec. 3.1, the laser spot used for 3D laser printing of photonic elements from the birefringent LCE resist is split into two foci, triggering a simultaneous polymerization of two separate voxels. This leads to a strong distortion of the shape of the structures, as exemplarily depicted in Fig. 6(c). Here, the SEM micrograph of a nominally disk-shaped WGM cavity shows two connected but distinct disks with an offset of several µm. The offset of the two foci is linearly depending on the focus depth of the ordinary excitation beam, as shown in Fig. 4. Consequently, this issue can be bypassed by adapting both the design of the photonic element as well as the configuration of the 3DLP system. Hereby, the focus depth of the ordinary excitation beam has to be minimized for all parts of the structure that need to be fabricated with high precision.

Regarding disk-shaped WGM cavities, this can be achieved rather simple, as schematically depicted in Fig. 5. On the left-hand side, the conventional 3DLP fabrication configuration is shown, which is leading to the pronounced double-disk shape (also see Fig. 6(c)) due to the laser beam's ordinary focus depth being set to around 30 μm by the resonator's pedestal height. The focus depth used to polymerize the resonator disk can be minimized by inverting the fabrication process with respect to the laser beam and adapting the cell's thickness to match the desired resonator height as sketched on the right-hand side of Fig. 5. Since the thickness of the cell can only be controlled down to a few μm, it has to be precisely determined within the 3DLP fabrication process. Based on that, the pedestal height of the resonator can be slightly adapted to further minimize the ordinary laser beam's focus depth down to very few μm. Figure 6(d) shows an SEM micrograph of a successfully fabricated WGM resonator following this approach. As it can be clearly seen, the double-disk character of the cavities was reduced to an extent where no harmful influence on their light-guiding properties is present.
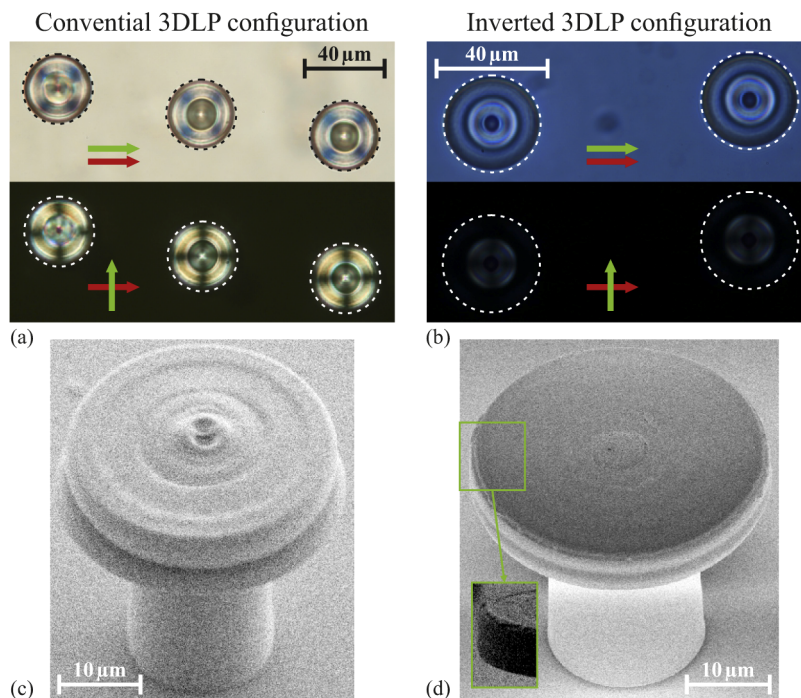

Fig. 6. Cross-polarizer and SEM micrographs of disk-shaped LCE cavities which were produced following different fabrication approaches. The cross-polarizer micrographs of the cavities fabricated via the inverted 3DLP configuration (b) show significantly less signal from the disks compared to the conventionally produced cavities (a), indicating a strongly enhanced mesogen alignment. Comparing the SEM micrographs, the double-disk character of the conventional cavities (c) was significantly reduced following the inverted 3DLP fabrication configuration (d). The inset in (d) presents a side view of the same cavity as in (d). The scale bar also applies to the inset.

Furthermore, the degree of mesogen alignment of the LCE in the resonator disk was strongly improved following the inverted fabrication approach, as it is clearly observable from cross-polarizer microscope images. While resonator disks printed in conventional 3DLP configuration show a rotationally symmetric distortion of the mesogen alignment (see Fig. 6(a)), a significantly better vertical alignment is found for cavities fabricated following our inverted approach (see Fig. 6(b)). We mainly attribute the alignment distortion of the conventionally produced cavity to

a varying shrinkage behavior of the two distinct disks caused by different intensities of the two separated foci and therefore different degrees of polymerization of the disks.

By the adaption of 3DLP fabrication configuration presented here, the focal depth of the fs-pulsed excitation laser beam was reduced to a few μm. Following this approach, we successfully realized the printing of high-resolution flexible photonic elements from LCE.

3.3. Reversible and full tunability of modes in resonators made from LCE

As an exemplary application of flexible photonic elements entirely made from LCE, we here present the successful realization of a fully tunable, high-quality WGM cavity printed by 3DLP. The tunability of the cavity was mediated by temperature and investigated by fiber-based transmission spectroscopy near the IR c-band (see also sec. 2.3).
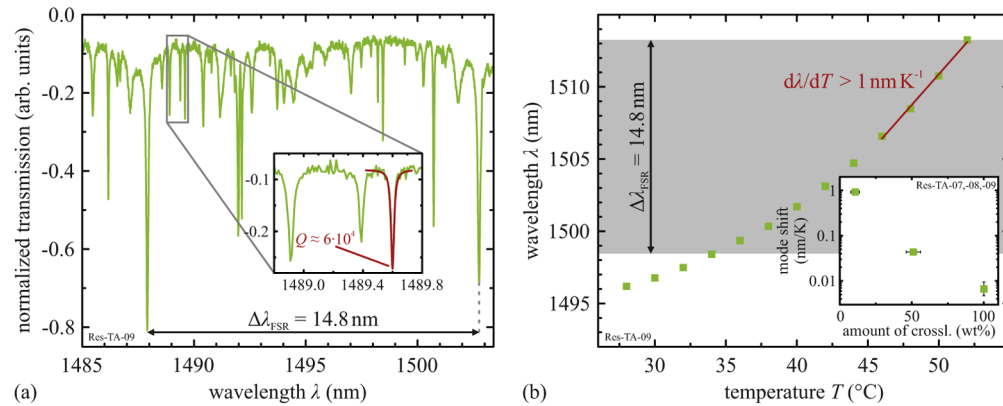

Fig. 7. (a) The fiber-based transmission spectrum of an LCE resonator made by 3DLP shows Lorentz-shaped resonance dips corresponding to whispering gallery modes with quality factors up to around 6×10^4 (see inset). The free spectral range $\Delta\lambda_{FSR}$ was determined to be around 14.8 nm. (b) For a temperature increase below 20 K, the temperature induced red shift of the spectral position of one WGM is larger than the free spectral range, demonstrating the cavity to be fully tunable at moderate temperatures. For small temperature ranges, the relative mode shift can be larger than $1\,\mathrm{nm\,K^{-1}}$ and is approximately linear. Inset: The relative mode shift can be tuned over more than two orders of magnitude by controlling the degree of crosslinking. This was accomplished by changing the LCEs molecular composition, i.e., the molecular share of the crosslinker molecule in the resist (also see sec. 2.1).

Various possible applications of WGM resonators like resonance filters [63] rely on a reversible and wide tunability of the cavities' resonant wavelengths. As apparent from their resonance condition $2\pi R \times n_{\mathrm{eff}} = N_\phi \times \lambda_0$, the resonant wavelength λ_0 of a WGM with a fixed azimuthal mode number N_ϕ can be reversibly tuned by either changing the effective refractive index n_{eff} or the cavity's radius R. Using resonators made from liquid crystal elastomers, both of these properties can be simultaneously changed using an external stimulus, which can lead to strong wavelength shifts. 3D laser printed tunable WGM resonators entirely made from LCE were already demonstrated by Nocentini *et al.* [37], who presented a WGM with a blue shift of around 30 % of its free spectral range under optical excitation. Compared to these cavities, the system presented here shows a significantly higher quality factor and increased tunability. These improvements are mainly attributed to the enhanced printing resolution and mesogen alignment achieved by solving the LCE resist in a eutectic nematic LC host as well as to the silanization process used here (for both see sec. 3.2).

The disk-shaped WGM cavities (also see SEM micrograph in Fig. 6(d)) were printed with nominal pedestal heights of 30 μm and radii of 25 μm, following the inverted fabrication

configuration introduced in sec. 3.2. Hereby, a scan speed of $4\,\mathrm{mm\,s^{-1}}$ and a relative laser power of 88 % were used.

Fig. 7(a) shows an exemplary fiber-based transmission spectrum of a WGM resonator 3D laser printed from LCE. Since the shown spectrum was measured in the regime of under-coupling, a lower bound of the intrinsic quality factor can be found to be around 6×10^4 via a Lorentzian fit. This finding corresponds to an improvement of the quality by a factor of more than 3 compared to previous results [37]. The free spectral range of $\Delta\lambda_{\mathrm{FSR}} = 14.8\,\mathrm{nm}$ equals to the minimum tuning range necessary to prove full tunability of the cavity. To investigate the tuning properties, the spectral position of a WGM resonance was identified via Lorentzian fits and tracked for different temperatures. Figure 7(b) shows the spectral mode position of one WGM over a temperature range of 24 K. A shift of the resonant wavelength over more than one free spectral range was achieved for temperature changes of around 18 K. Therefore, full tunability of the WGM cavity is successfully demonstrated. Additionally, the wavelength tuning is approximately linear for small temperature ranges of a few Kelvin and relative mode shifts of more than $1\,\mathrm{nm\,K^{-1}}$ were realized. Furthermore, the relative mode shift can be tuned over more than two orders of magnitude by changing the degree of crosslinking of the liquid crystal elastomer. This is exemplarily shown in the inset of Fig. 7(b), where the degree of crosslinking of the cavities was controlled via the molecular share of crosslinker (also see sec. 2.1).

The results presented here demonstrate the high potential of our newly developed approach to fabricate high-resolution 3D laser printed LCE structures. Furthermore, the strong and precisely controllable tunability of the geometrical and optical properties of such structures is shown.

4. Conclusion

In summary, we have successfully adapted 3D laser printing for the fabrication of flexible photonic elements based on liquid crystal elastomers (LCEs). We have described a method to print rigid polymer structures on flexible substrates made from in-plane aligned LCE. We have proven precise control of the distance between the rigid elements by calibrating the actuation strength of the LCE substrate using 2D marker arrays. The feasibility of these structures for photonic applications has been demonstrated by flexible coupling and decoupling of WGM resonator pairs. We also have developed a fabrication scheme for 3D laser printing of flexible elements entirely made from LCE. Within this context, we have conducted simulations of the light path of the fs-pulsed excitation laser beam in the birefringent LCE resist and have found a splitting of the laser focus into two simultaneously polymerizing foci. Based on these findings, we have developed an adaption of the conventional 3DLP fabrication configuration to bypass this issue. Fully tunable WGM resonators with high quality entirely made from LCE have been produced.

The reported fabrication methods combine the creative design options of 3D laser printing with the precisely controllable flexibility of liquid crystal elastomers and therefore establish a platform to realize complex architectures of tunable photonic elements.

Disclosures

The authors declare no conflicts of interest.

References

1. B. E. A. Saleh and M. C. Teich, *Fundamentals of photonics*, Wiley series in pure and applied optics (Wiley, Hoboken, NJ, 2019), 3rd ed.
2. R. Kirchain and L. Kimerling, "A roadmap for nanophotonics," Nat. Photonics **1**(6), 303–305 (2007).
3. H. Walther, B. T. H. Varcoe, B.-G. Englert, and T. Becker, "Cavity quantum electrodynamics," Rep. Prog. Phys. **69**(5), 1325–1382 (2006).
4. L. Lu, J. D. Joannopoulos, and M. Soljačić, "Topological photonics," Nat. Photonics **8**(11), 821–829 (2014).
5. M. Hochberg, N. Harris, R. Ding, Y. Zhang, A. Novack, Z. Xuan, and T. Baehr-Jones, "Silicon photonics: The next fabless semiconductor industry," IEEE Solid-State Circuits Mag. **5**(1), 48–58 (2013).
6. B. Jalali and S. Fathpour, "Silicon photonics," J. Lightwave Technol. **24**(12), 4600–4615 (2006).
7. R. Yan, D. Gargas, and P. Yang, "Nanowire photonics," Nat. Photonics **3**(10), 569–576 (2009).
8. P. N. Prasad, "Polymer science and technology for new generation photonics and biophotonics," Curr. Opin. Solid State Mater. Sci. **8**(1), 11–19 (2004).
9. T. Grossmann, M. Hauser, T. Beck, C. Gohn-Kreuz, M. Karl, H. Kalt, C. Vannahme, and T. Mappes, "High-Q conical polymeric microcavities," Appl. Phys. Lett. **96**(1), 013303 (2010).
10. P. Rabiei, W. H. Steier, C. Zhang, and L. R. Dalton, "Polymer micro-ring filters and modulators," J. Lightwave Technol. **20**(11), 1968–1975 (2002).
11. C.-S. Wu, C.-F. Lin, H.-Y. Lin, C.-L. Lee, and C.-D. Chen, "Polymer-Based Photonic Crystals Fabricated with Single-Step Electron-Beam Lithography," Adv. Mater. **19**(19), 3052–3056 (2007).
12. T. Wienhold, S. Krämmer, S. F. Wondimu, T. Siegle, U. Bog, U. Weinzierl, S. Schmidt, H. Becker, H. Kalt, T. Mappes, S. Koeber, and C. Koos, "All-polymer photonic sensing platform based on whispering-gallery mode microgoblet lasers," Lab Chip **15**(18), 3800–3806 (2015).
13. A. L. Martin, D. K. Armani, L. Yang, and K. J. Vahala, "Replica-molded high-Q polymer microresonators," Opt. Lett. **29**(6), 533 (2004).
14. O. Bar-On, P. Brenner, T. Siegle, R. Gvishi, H. Kalt, U. Lemmer, and J. Scheuer, "High Quality 3D Photonics using Nano Imprint Lithography of Fast Sol-gel Materials," Sci. Rep. **8**(1), 7833 (2018).
15. T. W. Kelley, P. F. Baude, C. Gerlach, D. E. Ender, D. Muyres, M. A. Haase, D. E. Vogel, and S. D. Theiss, "Recent progress in organic electronics: Materials, devices, and processes," Chem. Mater. **16**(23), 4413–4422 (2004).
16. H. Ma, A. Jen, and L. Dalton, "Polymer-Based Optical Waveguides: Materials, Processing, and Devices," Adv. Mater. **14**(19), 1339–1365 (2002).
17. Z. Zhang, P. Zhao, P. Lin, and F. Sun, "Thermo-optic coefficients of polymers for optical waveguide applications," Polymer **47**(14), 4893–4896 (2006).
18. Y. O. Noh, H. J. Lee, Y. H. Won, and M. C. Oh, "Polymer waveguide thermo-optic switches with −70 dB optical crosstalk," Opt. Commun. **258**(1), 18–22 (2006).
19. N. Tomczak, D. Jańczewski, M. Han, and G. J. Vancso, "Designer polymer-quantum dot architectures," Prog. Polym. Sci. **34**(5), 393–430 (2009).
20. J. Clark and G. Lanzani, "Organic photonics for communications," Nat. Photonics **4**(7), 438–446 (2010).
21. M. S. Luchansky and R. C. Bailey, "High-Q optical sensors for chemical and biological analysis," Anal. Chem. **84**(2), 793–821 (2012).
22. B. Wenger, N. Tétreault, M. E. Welland, and R. H. Friend, "Mechanically tunable conjugated polymer distributed feedback lasers," Appl. Phys. Lett. **97**(19), 193303 (2010).
23. P. Görrn, M. Lehnhardt, W. Kowalsky, T. Riedl, and S. Wagner, "Elastically Tunable Self-Organized Organic Lasers," Adv. Mater. **23**(7), 869–872 (2011).
24. S. Schauer, X. Liu, M. Worgull, U. Lemmer, and H. Hölscher, "Shape-memory polymers as flexible resonator substrates for continuously tunable organic DFB lasers," Opt. Mater. Express **5**(3), 576 (2015).
25. H. Feng, W. Shu, H. Xu, B. Zhang, B. Huang, J. Wang, W. Jin, and Y. Chen, "Two-directional tuning of distributed feedback film dye laser devices," Micromachines **8**(12), 362 (2017).
26. A. Berdin, H. Rekola, O. Sakhno, M. Wegener, and A. Priimagi, "Continuously tunable polymer membrane laser," Opt. Express **27**(18), 25634 (2019).
27. V. D. Ta, R. Chen, and H. D. Sun, "Tuning whispering gallery mode lasing from self-assembled polymer droplets," Sci. Rep. **3**(1), 1362 (2013).
28. T. Siegle, M. Remmel, S. Krämmer, and H. Kalt, "Split-disk micro-lasers: Tunable whispering gallery mode cavities," APL Photonics **2**(9), 096103 (2017).

29. T. Siegle, S. Schierle, S. Krämmer, B. Richter, S. F. Wondimu, P. Schuch, C. Koos, and H. Kalt, "Photonic molecules with a tunable inter-cavity gap," Light: Sci. Appl. **6**(3), e16224 (2017).

30. H. Zeng, P. Wasylczyk, C. Parmeggiani, D. Martella, M. Burresi, and D. S. Wiersma, "Light-Fueled Microscopic Walkers," Adv. Mater. **27**(26), 3883–3887 (2015).

31. M. Warner and E. M. Terentjev, *Liquid Crystal Elastomers*, International Series of Monographs on Physics (Oxford University Press, Oxford, UK, 2007), revised ed.

32. T. J. White and D. J. Broer, "Programmable and adaptive mechanics with liquid crystal polymer networks and elastomers," Nat. Mater. **14**(11), 1087–1098 (2015).

33. T. Ikeda and T. Ube, "Photomobile polymer materials: From nano to macro," Mater. Today **14**(10), 480–487 (2011).

34. H. Zeng, P. Wasylczyk, C. Parmeggiani, D. Martella, M. Burresi, and D. S. Wiersma, "Artificial Muscle: Light-Fueled Microscopic Walkers (Adv. Mater. 26/2015)," Adv. Mater. **27**(26), 3842 (2015).

35. D. Martella, S. Nocentini, D. Nuzhdin, C. Parmeggiani, and D. S. Wiersma, "Photonic Microhand with Autonomous Action," Adv. Mater. **29**(42), 1704047 (2017).

36. A. M. Flatae, M. Burresi, H. Zeng, S. Nocentini, S. Wiegele, C. Parmeggiani, H. Kalt, and D. Wiersma, "Optically controlled elastic microcavities," Light: Sci. Appl. **4**(4), e282 (2015).

37. S. Nocentini, F. Riboli, M. Burresi, D. Martella, C. Parmeggiani, and D. S. Wiersma, "Three-Dimensional Photonic Circuits in Rigid and Soft Polymers Tunable by Light," ACS Photonics **5**(8), 3222–3230 (2018).

38. A. Selimis, V. Mironov, and M. Farsari, "Direct laser writing: Principles and materials for scaffold 3D printing," Microelectron. Eng. **132**, 83–89 (2015).

39. F. Wang, L. Shao, Q. Bai, X. Che, B. Liu, and Y. Wang, "Photo-Induced Vertical Alignment of Liquid Crystals via In Situ Polymerization Initiated by Polyimide Containing Benzophenone," Polymers **9**(12), 233 (2017).

40. D. E. Schaub, "Dynamically Tunable Photonic Bandgap Materials The University of Manitoba," Ph.D. thesis, University of Manitoba (2010).

41. D. Nuzhdin, "High-Q microcavities: characterization and optomechanical applications," Ph.D. thesis, Universita degli Studi di Firenze (2018).

42. T. Beck, S. Schloer, T. Grossmann, T. Mappes, and H. Kalt, "Flexible coupling of high-Q goblet resonators for formation of tunable photonic molecules," Opt. Express **20**(20), 22012 (2012).

43. B. Peng, S. K. Özdemir, F. Lei, F. Monifi, M. Gianfreda, G. L. Long, S. Fan, F. Nori, C. M. Bender, and L. Yang, "Parity-time-symmetric whispering-gallery microcavities," Nat. Phys. **10**(5), 394–398 (2014).

44. S. Deng, W. Cai, and V. N. Astratov, "Numerical study of light propagation via whispering gallery modes in microcylinder coupled resonator optical waveguides," Opt. Express **12**(26), 6468 (2004).

45. J. K. S. Poon, J. Scheuer, Y. Xu, and A. Yariv, "Designing coupled-resonator optical waveguide delay lines," J. Opt. Soc. Am. B **21**(9), 1665 (2004).

46. H. Hodaei, A. U. Hassan, S. Wittek, H. Garcia-Gracia, R. El-Ganainy, D. N. Christodoulides, and M. Khajavikhan, "Enhanced sensitivity at higher-order exceptional points," Nature **548**(7666), 187–191 (2017).

47. W. Chen, J. Zhang, B. Peng, S. K. Özdemir, X. Fan, and L. Yang, "Parity-time-symmetric whispering-gallery mode nanoparticle sensor [Invited]," Photonics Res. **6**(5), A23 (2018).

48. J. Fischer and M. Wegener, "Three-dimensional optical laser lithography beyond the diffraction limit," Laser Photonics Rev. **7**(1), 22–44 (2013).

49. B. Peng, S. K. Özdemir, J. Zhu, and L. Yang, "Photonic molecules formed by coupled hybrid resonators," Opt. Lett. **37**(16), 3435 (2012).

50. T. Grossmann, "Whispering-gallery-mode lasing in polymeric microcavities," Ph.D. thesis, Karlsruhe Institute of Technology (2012).

51. J. C. Knight, G. Cheung, F. Jacques, and T. A. Birks, "Phase-matched excitation of whispering-gallery-mode resonances by a fiber taper," Opt. Lett. **22**(15), 1129 (1997).

52. L. Novotny and B. Hecht, *Principles of Nano-Optics* (Cambridge University Press, 2012), 2nd ed.

53. P. Török, P. Varga, Z. Laczik, and G. R. Booker, "Electromagnetic diffraction of light focused through a planar interface between materials of mismatched refractive indices: An integral representation," J. Opt. Soc. Am. A **12**(2), 325 (1995).

54. B. Richards and E. Wolf, "Electromagnetic diffraction in optical systems, II. Structure of the image field in an aplanatic system," Proc. Royal Soc. London. Ser. A Math. Phys. Sci. **253**, 358–379 (1959).

55. P. Yeh, "Electromagnetic propagation in birefringent layered media," J. Opt. Soc. Am. **69**(5), 742 (1979).

56. P. Yeh, *Optical Waves in Layered Media*, Wiley Series in Pure and Applied Optics (Wiley, 1988).

57. S. T. Wu, "Birefringence dispersions of liquid crystals," Phys. Rev. A **33**(2), 1270–1274 (1986).

58. J. Li, S. T. Wu, S. Brugioni, R. Meucci, and S. Faetti, "Infrared refractive indices of liquid crystals," J. Appl. Phys. **97**(7), 073501 (2005).

59. G. Abbate, V. Tkachenko, A. Marino, F. Vita, M. Giocondo, A. Mazzulla, and L. De Stefano, "Optical characterization of liquid crystals by combined ellipsometry and half-leaky-guided-mode spectroscopy in the visible-near infrared range," J. Appl. Phys. **101**(7), 073105 (2007).

60. S. Nocentini, "Tunable polymeric photonic structures," Ph.D. thesis, Universita degli Studi di Firenze (2016).

61. A reasonable comparison of the mechanical and optical properties of LCE structures polymerized via 1-photon (see sec. 2.1) and multi-photon (see sec. 3.2) absorption is not possible here, since these structures also differ in their order of size, shape, preferential mesogen alignment direction relative to the glass cell, as well as alignment mechanism.

62. C. C. Tartan, P. S. Salter, T. D. Wilkinson, M. J. Booth, S. M. Morris, and S. J. Elston, "Generation of 3-dimensional polymer structures in liquid crystalline devices using direct laser writing," RSC Adv. **7**(1), 507–511 (2017).

63. V. S. Ilchenko and A. B. Matsko, "Optical resonators with whispering-gallery modes - Part II: Applications," IEEE J. Select. Topics Quantum Electron. **12**(1), 15–32 (2006).